Published by Oxford University Press
on behalf of the United States Government, 2009.

Journal of Electron Microscopy **58(3)**: 87–97 (2009)
doi: 10.1093/jmicro/dfn030

Special number: History/Review

Atomic-resolution spectroscopic imaging: past, present and future

Stephen J. Pennycook[1,2,*], Maria Varela[1], Andrew R. Lupini[1], Mark P. Oxley[1,2] and Matthew F. Chisholm[1]

[1]Materials Science and Technology Division, Oak Ridge National Laboratory, PO Box 2008, Oak Ridge, TN 37831-6030 and [2]Department of Physics and Astronomy, Vanderbilt University, Nashville, TN 37235, USA
*To whom correspondence should be addressed. E-mail: pennycooksj@ornl.gov

Abstract This review examines the development of atomically resolved electron energy loss spectroscopy from the first demonstration of plane-by-plane compositional profiling, through column-by-column spectroscopy to full two-dimensional and potentially three-dimensional spectroscopic imaging. Examples will be presented to highlight the increasing analytical sensitivity and image contrast obtained through each generation of aberration correction, moving towards the ultimate goal of mapping electronic structure inside materials with atomic resolution.

Keywords annular dark field, column-by-column spectroscopy, electron energy loss, scanning transmission electron microscopy, spectroscopy

Received 15 September 2008, accepted 9 December 2008, online 21 January 2009

Introduction

One of the key advantages of a scanning microscope is that any signal that varies with probe position can, in principle at least, be collected and used to form an image. Since the early development of the scanning transmission electron microscope (STEM), the advantages of simultaneous annular dark-field (ADF) imaging, also referred to as *Z*-contrast imaging, and electron energy-loss spectroscopy (EELS) have been recognized [1]. The very different angular distributions of the elastic (or thermal diffuse) scattering and inelastic scattering mean that both signals can be collected simultaneously with a reasonable efficiency using different detectors, low- to medium-angle inelastic scattering through an axial spectrometer and high-angle scattering with the annular detector. Since the fine structure on core-loss spectra reflects the local density of electronic states (in the presence of the core hole), it has always been understood that the combination of imaging and EELS should, in principle, allow atomic resolution mapping of a material's electronic structure.

It is most convenient if the elastic and inelastic images both show incoherent characteristics and specifically, no contrast reversals with specimen thickness or objective lens focus as are characteristic of coherent phase contrast images. Then the ADF image can be used to locate the probe for EELS. Note that in this review, for clarity we will refer to the ADF image as elastic whether it is truly elastic (Bragg) scattering or quasielastic (thermal diffuse) scattering. It can be shown mathematically that if all the inelastically scattered electrons are detected then an incoherent image is obtained [2,3]. In practice, incoherent characteristics dominate whenever the EELS collection aperture is comparable in size to the probe-forming aperture. Before aberration correction it was relatively simple to achieve collection angles two or three times the probe semiangle, but in aberration-corrected systems the greatly increased probe-forming aperture has made this difficult to achieve in some cases. If collection angles are significantly smaller than the probe semiangle then complications arise from phase-contrast effects and effective nonlocal inelastic interactions, as we discuss later.

With new generations of microscopes, such difficulties are rapidly being overcome, and there is no doubt that the advent of aberration correction has enormously advanced the practical application of spectroscopic imaging. By dramatically reducing the size of the electron probe, more current can be focused on an atom or atomic column of interest with less wasted illuminating neighboring columns, provided the specimen is sufficiently thin that geometric probe broadening is not an issue. The result is not just improved resolution, but higher signal-to-noise and signal-to-background ratios, with reduced beam damage and greatly enhanced detectability. This advance has brought the ability to image and identify single atoms in single atomic columns inside materials for the first time [4]. Of course, these benefits are only

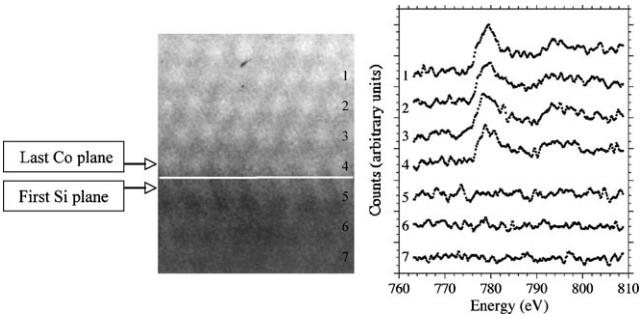

Fig. 1. A representative *Z*-contrast image of a $CoSi_2$/Si {111} interface with spectra obtained plane by plane across the interface, marked with a white line. The first Si plane shows dumbbells in a twin orientation. The image is scanned from the original Polaroid taken in 1993 using a VG Microscopes (East Grinstead, UK) HB501UX STEM operating at 100 kV. Spectra were recorded using a parallel EELS system designed by D. McMullen described in the text. Spectra 1–4 are background-subtracted by the usual power-law fit, spectra 5–6 are obtained using the spatial difference method, using a reference spectrum from Si far from the interface. Because of the twin, the distance between planes 4 and 5 is 2.7 Å. Data do not necessarily correspond with the precise area shown in the image, but are from the respective planes as numbered on the plot, adapted from [22,24].

obtained in thin samples; in thicker samples beam broadening significantly degrades the spatial resolution.

In addition to these improvements in sensitivity, the larger probe-forming aperture results directly in reduced depth of field, which has been used to locate individual atoms in three dimensions by optical sectioning [5–8]. In principle, the same methods should be applicable to EELS [9]. In addition, a true confocal mode of operation has been demonstrated and appears to offer significant advantages for depth resolution especially of extended objects [10–12].

Plane-by-plane spectroscopy

The first demonstration of atomic-resolution spectroscopy was in 1993, with Co *L* edge spectra taken plane by plane across an atomically abrupt $CoSi_2$/Si {111} interface, as shown in Fig. 1. Spectra were recorded with the beam scanning a line parallel to the interface, averaging over many unit cells in the scan direction but maintaining an atomic resolution perpendicular to the interface. Therefore, this experiment represents an edge resolution test [13]. In a continuum model, convolving a Gaussian resolution function with a step function object results in a curve that drops from 75 to 25% in a distance equal to the full-width-half-maximum (FWHM) of the Gaussian. In the *Z*-contrast image, the Co atoms (atomic number, $Z = 27$) show brightest (as circles) while the Si atoms ($Z = 14$) are much darker. The Si dumbbells are unresolved, but recognizably elongated so that the position of the interface is unambiguous. This system was specifically chosen because it was well known at the time to form atomically abrupt interfaces over long distances, free from steps or protrusions [14–20]. This has also been confirmed more recently, see [21]. For spectroscopy, the scan was rotated until the fast scan direction was parallel to the interface and then the probe was switched to the line scan mode, which could then be centered accurately on each plane in turn by reference to the simultaneous ADF intensity displayed on an oscilloscope [22]. In this way any spatial drift during spectral acquisition would be seen. Spectra were obtained plane by plane across the interface as shown in Fig. 1, and clearly exceed the 50 percentage point drop required by the edge resolution test.

The parallel EELS system was designed by Dr Dennis McMullan of the Cavendish Laboratory and was specifically optimized for the high detection sensitivity required for column-by-column spectroscopy [23]. The system was based on a Wright Instruments charge-coupled-device (CCD) camera, using a thinned, multi-phase-pinned CCD chip, which had a sensitivity double that of the normal chip. More importantly, this chip had a very low noise level (0.05 electrons) and read-out noise (2 electrons) which was practically negligible compared to the estimated 10 CCD charges per 100 kV electron. The chip was a two-dimensional (2D) array that could be binned over typically 50 channels in the non-dispersive direction, and was optically coupled by large-aperture Rodenstock lenses to the scintillator. Therefore, the system was essentially free from channel-to-channel gain variations, which can be a problem with the fiber-optic coupled designs common today.

Spectra were initially background-subtracted by the normal power-law method fitting to a window of ~38 eV ahead of the Co *L* edge [24]. Subsequently, we applied the spatial difference method [25] to those spectra with the least Co, spectra 5–7. (An inconsistency in the original figure caption has been recently corrected [26]). Based on the method of [27], using the actual counts in the spectrum files, we estimate today a background extrapolation error of ±4%, whereas in 1993 we estimated the total error to be ±10%. The original profile is shown in Fig. 2 and compared to a modern reanalysis of the data using a least-squares routine and to a simulated spectroscopic image [28]. The agreement between the original analysis, the reanalysis and the simulation is well within the error bars estimated at the time and clearly confirms atomic resolution.

Comparing to the original background subtraction method, the modern reanalysis shows that the spatial difference method removed roughly 10 percentage points of Co from spectra 5–7, which did not alter the demonstration of atomic resolution, but was appropriate since surface Co would be expected to result from the ion-milling procedure used to prepare the cross section. Application of the spatial difference method to the silicide spectra would of course have been inappropriate. For comparison with this atomically abrupt interface, we also took a profile across a two-plane wide interface, which is shown in Fig. 3 [29]. This $CoSi_2$/Si {100} interface shows a reconstruction with every other Co column missing from the last Co-containing plane. The EELS concentration extracted from this plane is around

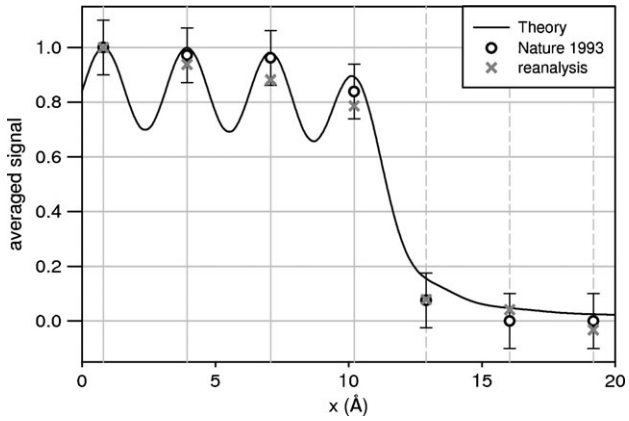

Fig. 2. Co composition profiles obtained from the 1993 data compared to dynamical simulations. The original data points from the 1993 *Nature* paper are shown as black circles with the ±10 percentage point error bars estimated in 1993. A reanalysis of the associated spectra using a modern least-squares fitting routine is shown as gray crosses, and a simulation for a sample thickness of 100 Å is indicated by the black solid line. Both agree well with the original analysis. The simulation used a 10.3-mrad probe-forming aperture, a spherical aberration coefficient of 1.3 mm and Scherzer defocus of −693 Å. Ionization scattering coefficients assumed a detector of 30-mrad semiangle and a 30-eV energy window above threshold. The solid vertical gray lines indicate the planes within the $CoSi_2$ with the Si planes indicated by the vertical dashed gray lines.

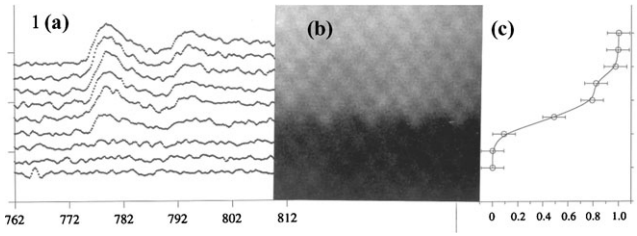

Fig. 3. Atomic-resolution EELS profile across a two-plane wide $CoSi_2$/Si {100} interface. The image shows a half-occupied interfacial plane and the EELS analysis is ∼50% of the bulk. Reproduced from photographs used in the preparation of [29].

50%, as would be expected from the image. These data were obtained in exactly the same way as the previous results using the same system. The key to the success of these experiments was very careful sample preparation, coupled with the fact that Si is light and generates minimal beam broadening. A later example of plane-by-plane compositional analysis of a NiO–ZrO_2 interface is presented in Fig. 4 [30], where the composition profile is slightly broader due to the higher atomic number of the elements involved and/or to a thicker sample. Surprisingly, plane-by-plane spectroscopy was not widely taken up, perhaps due to the limited availability of suitable EELS systems. An alternative approach is to normalize out the lattice contrast to see only longer range changes in composition or electronic structure, see for example [31].

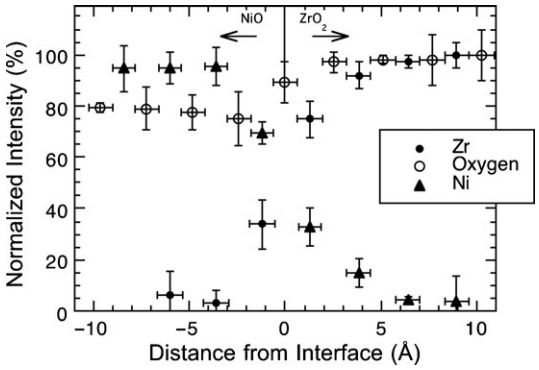

Fig. 4. EELS profiles recorded plane by plane across the NiO–ZrO_2(cubic) interface showing the presence of a common oxygen plane at the interface. Data taken with the uncorrected VG Microscopes HB501UX with McMullen PEELS system, reproduced from [30].

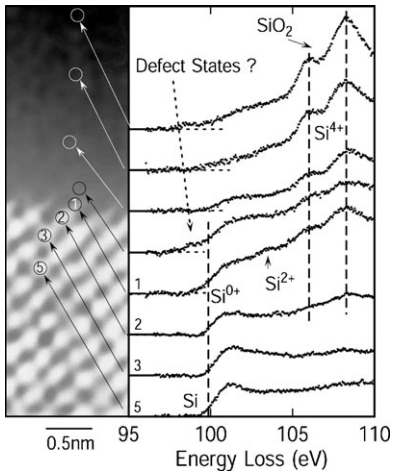

Fig. 5. Column-by-column spectroscopy at the Si/SiO_2 interface showing a pre-edge feature at the interface which is not seen from spectrum 1 ∼2 Å away. Reproduced from [32] with permission.

Column-by-column spectroscopy

For atomic column-by-column spectroscopy, the probe is either stopped over a column of interest selected from the *Z*-contrast image or scanned over a very small region centered on the column. The first demonstration of atomic column-by-column spectroscopy was also in 1993, as reproduced in Fig. 5 [32]. In his paper, Batson did not claim atomic column resolution, stating 'although these spectra certainly identify scattering due to columns of unit cells (0.53 nm) of Si, they do not yet reflect clean analytical signals from individual columns of atoms'. However, the pre-edge feature identified as defect states in the figure is absent from the column of Si only ∼2 Å away, and Batson says later in the paper that his results 'certainly change on a length scale commensurate with atomic column spacings'. Since the Si columns 1–5 give identical spectra, strictly speaking column-by-column spectroscopy could not be demonstrated with this sample. However, given the change in EELS fine

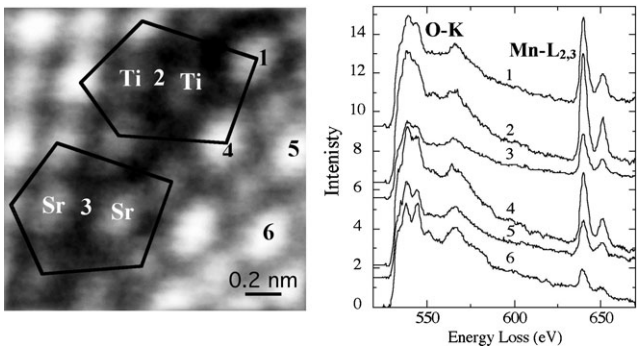

Fig. 6. (a) *Z*-contrast image from a Mn-doped 36° $SrTiO_3$ grain boundary recorded under an uncorrected 300-kV VG Microscopes HB603U STEM. (b) EELS spectra recorded by stopping the probe on the corresponding atomic columns, revealing differences in the Mn concentration and valence at different sites. Data recorded under an uncorrected 100-kV VG Microscopes HB501UX STEM with McMullan parallel EELS system. Reproduced from [38].

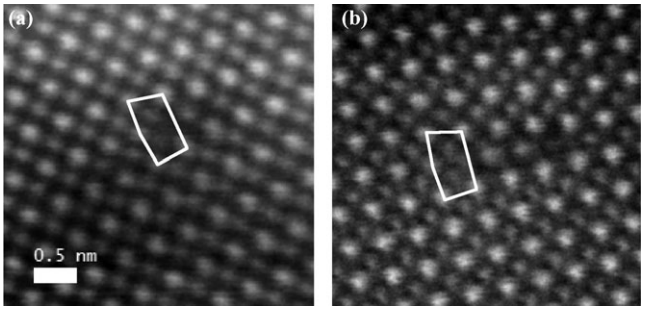

Fig. 7. Structural differences in pristine and Ca-doped YBCO. (a) *Z*-contrast image of pristine 4° [001] tilt grain-boundary dislocation core on the Cu–O sublattice, showing the typical pentagonal arrangement. (b) Ca-doped grain boundary: the Y/Ba column pentagonal arrangement now encircles three columns, two on the Cu–O and one on the Y/Ba sublattice. Note the weaker intensity of the Y/Ba column on the left of the core, due to Ca substitution, and the extensive changes in the intensity of the CuO columns to the right of the core, due to substitution of Ba (brighter columns) and Ca (darker columns). EELS verified the compositional changes suggested from the image. Reproduced from [46].

structure from the amorphous SiO_2 to column 1, a distance of only ~2 Å, it would seem that this experiment did in fact achieve sufficient resolution to resolve individual Si dumbbells (pairs of columns). At the time, however, the issues of probe channeling and dechanneling, and of delocalization of the inelastic excitation [3,33], were not so well understood as they are today. Now we know that atomic resolution is possible at low lying edges such as the Si $L_{2,3}$ edge at around 100 eV, but the *contrast* is reduced due to an extended tail on the response, as we show later. Therefore, with the benefit of hindsight, we feel Batson's paper marks the first demonstration of atomic column spectroscopy. With the $CoSi_2$/Si interfaces it was not possible to obtain atomic column resolution using the Co $L_{2,3}$ edge at ~776 eV due to beam damage, which was the reason for scanning the probe for several nanometers parallel to the interface during the 5-s acquisition time.

Also in 1993 was the first demonstration of 2D mapping using EELS fine structure, using the π^* and σ^* peaks at the C *K* edge to map sp^2 and sp^3 bonded carbon. The transition from sp^2 to sp^3 carbon was seen to occur over less than a nanometer [34].

Column-by-column spectroscopy was subsequently widely applied to interfaces and grain boundaries, see for example [35–37]. An example of the first spectroscopic identification of impurity segregation to specific atomic sites in a grain boundary is shown in Fig. 6 [38]. The Mn impurity is not detectable in the image, but the spectra show that it prefers to occupy the Ti site in the grain boundary core, where its valence, determined from the ratio of the Mn L_3 and L_2 peaks [39–43], is close to the +3 formal oxidation state instead of the +4 state expected for a stoichiometric boundary. Later studies confirmed that grain boundaries in $SrTiO_3$ are intrinsically non-stoichiometric, which is the underlying cause of their electrical activity [44].

With the successful implementation of aberration correction in STEM [45], the contrast in both ADF and spectroscopic images of $SrTiO_3$ and related complex oxides was greatly increased. A spectacular success of the aberration-corrected system has been the identification of the mechanism whereby Ca enhances the grain boundary critical current in $YBa_2Cu_3O_{7-x}$ (YBCO) by a combination of *Z*-contrast imaging, column-by-column spectroscopy and first-principles theory [46]. In an undoped material, grain boundaries have a catastrophic effect on critical current, giving an exponential decrease with increasing grain boundary misorientation [47–49]. The grain boundaries showed the same core structures as in the prototypical $SrTiO_3$, and studies using bicrystals showed that the grain boundary structures followed the same structural unit model [50]. Assuming non-stoichiometry as in the case of $SrTiO_3$ would again lead to band bending, and the width of the depletion zone was predicted to increase linearly with grain boundary misorientation. The supercurrent is therefore forced to tunnel through this non-superconducting zone at the grain boundary, naturally explaining the exponential reduction in critical current [51,52]. With aberration correction, the non-stoichiometry could be followed on a column-by-column basis for the first time. Figure 7 shows that the doped dislocation cores have a different core structure, more extended than in the undoped material [53]. In particular, many columns showed anomalous intensities, which were investigated through column-by-column EELS. In YBCO, the threshold for beam damage is simple to assess because the pre-peak on the O *K* edge is directly related to the local hole concentration [54]. The dose per atomic column (exposure time and beam current) was adjusted so that no change occurred in the O pre-peak during spectrum acquisition. Because the sample was a bicrystal, with an

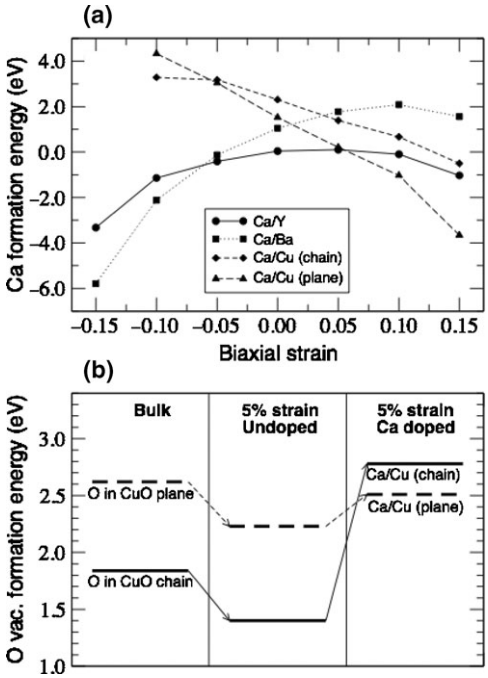

Fig. 8. First-principles calculations of Ca and O vacancy formation energy in bulk YBCO. (a) Energy required for substituting Ca on different lattice sites in YBCO as a function of biaxial strain. It is energetically more favorable for Ca to replace Y, Ba or Cu, depending on the local strain. (b) Formation energy of O vacancies in bulk YBCO (left panel), undoped YBCO under 5% tensile strain in a–b plane (central panel) and Ca-doped YBCO under 5% tensile strain (right panel), simulating the expanded regions at grain boundaries. For doped grain boundaries where Ca substitutes for Cu, the O vacancy formation energy increases significantly. Reproduced from [46].

array of identical core configurations, spectra were then summed from a sufficient number of dislocation cores (five) to achieve the statistics required [46].

The segregation phenomenon was found to be far more complex that previously supposed. It was originally assumed that at the grain boundary, as in the bulk, Ca (+2) would segregate for Y (+3) thereby donating holes to the grain boundary to compensate the intrinsic hole depletion. However, in the highly strained region of the dislocation core, it was found instead that Ca substituted for Ba in regions of compression and for Cu in regions of tension. By substituting a smaller atom in the compressed region and a larger atom in the tensile region, the local stresses would be reduced, the driving force for the O depletion would be reduced, and indeed, EELS showed O concentrations to increase to bulk values at most (but not all) of the sites. Theory was in full accord with the experiment, as shown in Fig. 8, predicting O vacancy formation energies would be restored to near bulk values. Hence the mechanism involves a cooperative doping phenomenon driven by the large strain fields of the dislocation core.

The ultimate column-by-column EELS analysis was also achieved as a result of aberration correction, the spectroscopic identification of a single La atom in a specific atomic

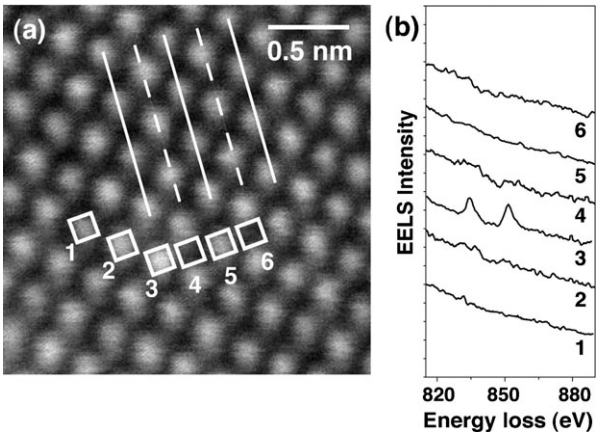

Fig. 9. Spectroscopic identification of an individual atom in its bulk environment by EELS. (a) *Z*-contrast image of $CaTiO_3$ showing traces of the CaO and TiO_2 {100} planes as solid and dashed lines, respectively. A single La dopant atom in column 3 causes this column to be slightly brighter than other Ca columns, and EELS from it shows a clear La $M_{4,5}$ signal. (b) Moving the probe to adjacent columns gives reduced or undetectable signals. Data recorded using the VG Microscopes HB501UX with Nion aberration corrector and McMullan PEELS system, adapted from [4].

column in $CaTiO_3$ [4], as shown in Fig. 9. The specimen was grown especially for the experiment with a series of La-doped layers of decreasing concentration at known distances from the substrate. Single atoms could be detected in the *Z*-contrast image, and results from many atoms all gave similar results, indicating single-atom sensitivity. Spectra were acquired for several tens of seconds by scanning a region ~1 Å × 1 Å. Despite a collection efficiency of only 8%, the La $M_{4,5}$ peaks are clearly visible in the spectrum from the La-containing column, and a residual signal is also seen from adjacent columns. The residual signal is due to beam broadening and through dynamical simulations the depth of the atom was estimated to be ~120 Å. Recently, an analysis of the expected signal-to-noise ratio for this experiment was performed by Krivanek *et al.* [55], predicting a 4:1 ratio of the La M_5 peak height to the peak-to-peak background noise, in good agreement with the data shown in Fig. 9.

Atomic-resolution spectroscopic imaging: elemental mapping

Spectroscopic imaging of single atoms was in fact first achieved in an uncorrected microscope. Suenega *et al.* [56] showed images of individual Gd atoms encapsulated in a carbon nanotube. The Gd atoms were sufficiently widely spaced so that they could be imaged individually with ~6 Å resolution using the Gd $N_{4,5}$ edge at 140 eV. With aberration correction, however, line scans could be readily achieved across crystal unit cells clearly resolving the atomic columns for the first time [57]. Now issues such as ionization delocalization could be investigated with much greater sensitivity and compared to dynamical simulations. Figure 10

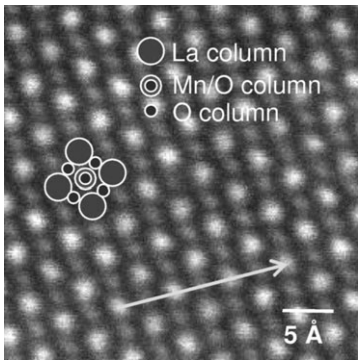

Fig. 10. *Z*-contrast image of $LaMnO_3$ in the pseudocubic ⟨100⟩ zone axis. The arrow indicates the [110] direction. Reproduced from [58].

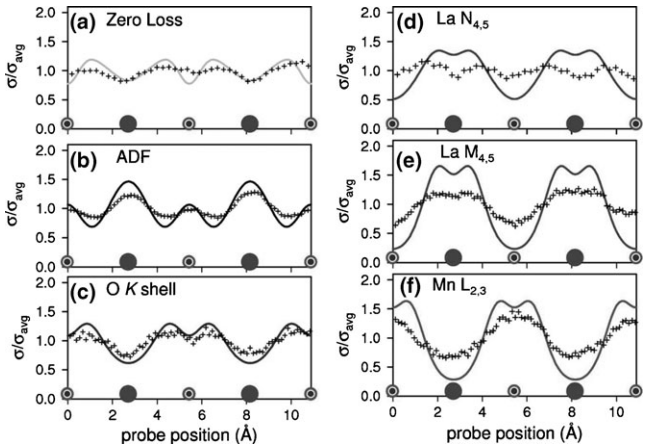

Fig. 11. Experimental [110] line scans (crosses) and simulations (solid lines) for (a) the zero-loss peak, (b) annular dark field, (c) the O *K* edge, (d) the La $N_{4,5}$ edge, (e) the La $M_{4,5}$ edge and (f) the Mn $L_{2,3}$ edge. The positions of the atomic columns are indicated by the circles, as in Fig. 10. Data recorded with the VG Microscopes HB501UX equipped with Nion aberration corrector and Gatan Enfina PEELS system, reproduced from [58]

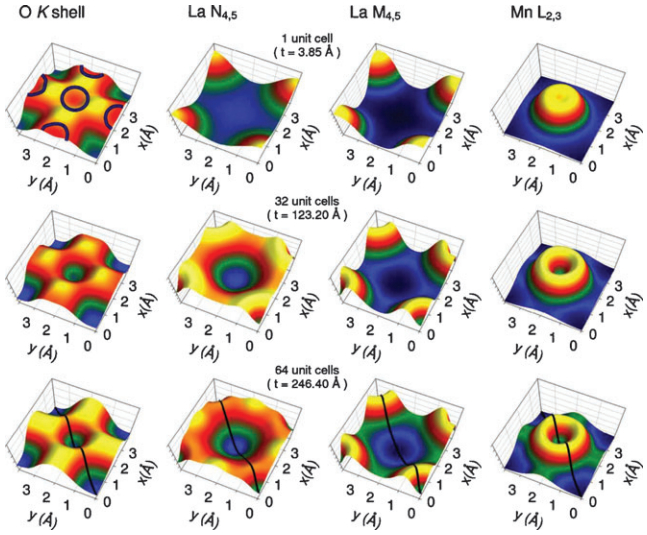

Fig. 12. Two-dimensional EELS simulations for the O *K* edge, the La $N_{4,5}$ edge, the La $M_{4,5}$ edge and the Mn $L_{2,3}$ edge as a function of specimen thickness, showing the formation of volcano-like structures on the O and MnO columns (blue circles) even in a specimen one-unit-cell thick. With increasing thickness the intensity of the MnO column in the center of the cell reduces due to depletion of the beam by scattering from the Mn, and a volcano feature develops in the Mn $L_{2,3}$ and La $M_{4,5}$ images. The low-energy La $N_{4,5}$ edge shows atomic resolution, although a long-range tail exists due to delocalization. Black lines indicate the [110] directions corresponding to the line scans in Fig. 11. Reproduced from [58].

shows a *Z*-contrast image of $LaMnO_3$ in the pseudocubic ⟨100⟩ zone axis. Experimental EELS line scans were taken along the [110] direction passing through La and MnO columns as shown in Fig. 11 [58]. All experimental data show reduced contrast compared to simulations, as commonly found in high-resolution TEM images [59]. The zero-loss image shows generally inverted contrast with respect to the ADF image, as expected. However, neither the shape nor the width of the inelastic images shows a simple dependence with inner-shell binding energy as has often been assumed in the past.

The ionization delocalization distance proposed by Egerton [27] is

$$d_{50} = 0.5\lambda/\theta_E^{3/4} \qquad (1)$$

where d_{50} is the diameter containing 50% of the inelastic excitations and $\theta_E = \Delta E/2E$, where ΔE is the energy loss and E the energy of the fast electron. The shape of the response function, based on a semiclassical description of the excitation, is given in Fig. 4 of [60], where it can be seen that the FWHM of the response is at approximately half the value of d_{50}. This is an excellent rule of thumb under incoherent conditions (collection of all or most of the scattered electrons) but does not take account of dynamical effects or effective non-local interactions, which are evident in Fig. 11. Compare for example the experimental profile of the La $N_{4,5}$ edge at ~99 eV to that obtained with the La $M_{4,5}$ edge at ~842 eV (Fig. 11d and e). The contrast observed at the La $N_{4,5}$ edge is much weaker, roughly half of that observed at the La $M_{4,5}$ edge, and the volcano feature is larger than expected from the theoretical trace, but the trace clearly shows contrast with the periodicity of the unit cell well above the noise of the data. The d_{50} values predicted by Eq. (1) are 5.5 Å and 1.1 Å, respectively, whereas experimentally and theoretically the FWHM are very similar. Therefore, atomic resolution is observed at both edges, but the *contrast* of the La $N_{4,5}$ edge is reduced in comparison to the La $M_{4,5}$ line trace due the extended tail of the La $N_{4,5}$ response function.

2D spectroscopic image simulations make the situation much clearer, and also show additional effects due to dynamical (channeling) effects and the effective non-local inelastic interaction [58]. In Fig. 12, the top row of simulations shows images from a crystal one-unit-cell thick, where there are negligible dynamical effects on the probe intensity. The shape of the inelastic response function can be easily

appreciated, and in both the La $N_{4,5}$ and $M_{4,5}$ images, peaks are seen on the La columns. Besides the small difference in width of the peaks, there is a significant difference in the response at the center of the cell, far from the columns, where the La $N_{4,5}$ response is still almost half its level at the columns. In the case of the La $M_{4,5}$ image, the response at the center of the cell is close to zero. This is in complete accord with the experimental line traces in which the La $N_{4,5}$ image shows about half the contrast of the La $M_{4,5}$ image. It is also in agreement with Eq. (1), since indeed much of the La $N_{4,5}$ response does lie far from the atom.

The simulated O K images show volcano-like features on the atom sites that are due to effective non-local interactions (see also [61]). Such features tend to appear when the collection angle of the spectrometer is significantly less than that of the probe-forming aperture, and are visible in the experimental line trace in Fig. 11. In thicker crystals, a big difference becomes apparent between the columns containing only O and those containing Mn in addition (those in the center of the cell). As Mn is much heavier than O, with an increasing thickness more of the beam is scattered to higher angles, and the electrons are lost to the EELS image. This dechanneling phenomenon makes this column appear darker in the EELS image than the other O columns. Interpretation of spectroscopic images must always take into account contrast due to elastic scattering. Similar volcano effects are seen on the La $N_{4,5}$ and Mn $L_{2,3}$ simulated images for the thicker cases, again due to dechanneling. These simulations show clearly that neither d_{50} nor $d_{50}/2$ should be interpreted as the FWHM of a Gaussian blur, as is sometimes assumed. These represent good order of magnitude estimates for, respectively, the mean interaction distance and the FWHM of the image peak, but cannot predict the detailed form of the contrast for which accurate quantum mechanical simulations are necessary.

Recently, the first experimental 2D spectroscopic images have appeared using a third-order aberration-corrected STEM [62], and even using an uncorrected microscope with a long acquisition time [63]. An example of a 2D spectroscopic image of $SrTiO_3$ in the ⟨110⟩ projection obtained with a VG Microscopes HB603U is shown in Fig. 13. The length of the microscope column was extended and a custom-designed objective lens winding was used to allow the whole bright-field disk to be admitted to the spectrometer without the use of additional coupling modules. The Ti L spectroscopic image shows peak intensities centered over the Ti columns as determined by the simultaneously acquired Z-contrast image. In the case of the O image, peak intensities are seen over the pure O columns (where the ADF intensity is weakest) but the Sr/O columns are not visible due to the enhanced scattering to high angles.

Much higher signal levels are available in the new fifth-order aberration-corrected STEMs. Figure 14 shows 2D spectrum images obtained with the Nion (Kirkland, Washington, USA) UltraSTEM operating at a 100-kV accelerating voltage. The image shows a misfit dislocation core at a $SrTiO_3/CaTiO_3$ interface and the color-coded Ca/Ti map indicates changes in the detected ratio that may either indicate some segregation or may just be a contrast effect. Both the O and Ti maps are continuous across the interface indicating that beam damage was not a problem. The availability of 100% signal collection with flexible illumination conditions opens up the potential to investigate bonding details in materials

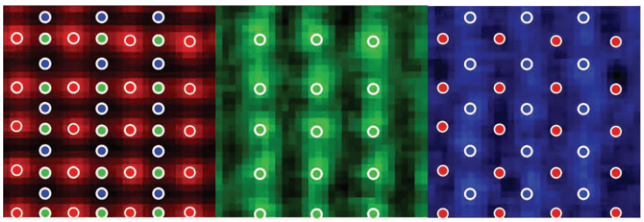

Fig. 13. Two-dimensional spectrum imaging of $SrTiO_3$ in the ⟨110⟩ projection using the VG Microscopes HB603U with Nion aberration corrector and Gatan Enfina operating at 300 kV. The left-hand panel (red) shows the Z-contrast image with the Sr/O, Ti and O columns shown as red, green and blue circles. The center and right-hand panels show the integrated signal from the simultaneously acquired Ti L and O K edges (40-eV integration windows were used with a large 260-eV background fitting window to reduce possible artifacts). In the O image, the pure O columns (blue) are seen bright but the Sr/O columns (red) are not visible. The convergence angle was ~25 mrad, and a beam current of ~50 pA and an exposure time of 0.025 s per pixel were chosen to minimize damage. Images recorded by A. R. Lupini and M. F. Chisholm.

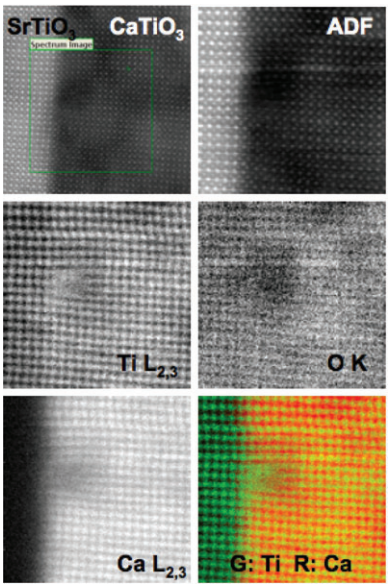

Fig. 14. Spectrum images obtained with the fifth-order-corrected Nion UltraSTEM operating at a 100-kV accelerating voltage. The images show a misfit dislocation core at a $SrTiO_3/CaTiO_3$ interface. The Ca, O and Ti maps are shown after principal component analysis. Ti and O maps and are seen to be continuous across the interface. The color-coded Ca/Ti ratio map shows some contrast at the dislocation core. Maps are 128 × 128 pixels, acquisition time is 0.01 s/pixel and beam current ~200 pA. Background was subtracted using a power-law fit and integration windows of ~15 eV were used. Images recorded by M. Varela and M. F. Murfitt, adapted from [76].

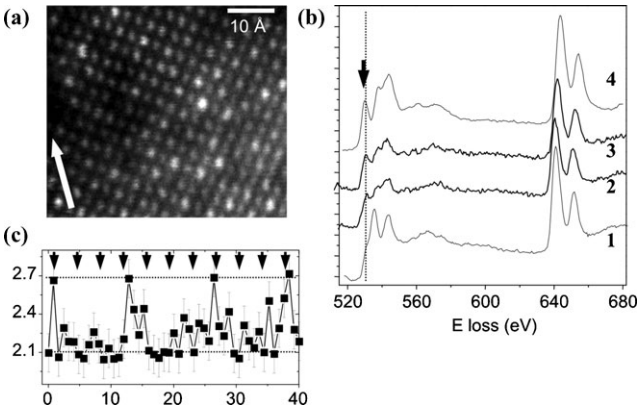

Fig. 15. (a) *Z*-contrast image of BCMO showing Bi dopant atoms as bright spots. (b) Electron energy-loss spectra typical of a $Mn^{+3}O$ column (2) and a $Mn^{+4}O$ column (3). Spectrum (4) comes from $CaMnO_3$, while (1) corresponds to bulk $LaMnO_3$. The oxygen *K* edge (around 530 eV) and the Mn *L* edge (around 644 eV) are shown. (c) $L_{2,3}$ ratio along the direction marked with an arrow in (a). Horizontal lines represent the $L_{2,3}$ ratio expected for a pure Mn^{+3} oxidation state (top) and a pure Mn^{+4} oxidation state (bottom). The positions of Mn planes along the scan have been marked with arrows. Data recorded using the VG Microscopes HB501UX with Nion aberration corrector and McMullan PEELS system, adapted from [65].

at atomic resolution, as shown by the recent 2D maps of a $La_{0.7}Sr_{0.3}MnO_3/SrTiO_3$ multilayer that were taken using only a single 0.5 eV wide window in Ti and Mn L_3 edges, see Supporting Online Material for ref. [64].

Atomic-resolution spectroscopic imaging: mapping of electronic structures at sub-unit cell resolution

Atomic-scale mapping of near-edge structures is clearly feasible on the new generation of aberration-corrected STEMs at a sub-unit cell level of resolution. However, interpretation of contrast variations in terms of local electronic structure at this level of resolution requires all non-local and dynamical effects to be modeled successfully. The manganites offer an unprecedented potential for exploring such effects, as we have shown above, and the results are immediately of major interest in understanding the plethora of unexpected properties seen at interfaces between different manganite phases. EELS has the potential to distinguish compositional intermixing from local charge transfer processes, and to probe the spatial extent of such effects at individual interfaces within a superlattice structure. An early example of the potential for such studies is shown in Fig. 15 at a unit-cell level of resolution. A *Z*-contrast image of a $Bi_xCa_{1-x}MnO_3$ (BCMO) manganite with $x = 0.37$ shows randomly located bright spots corresponding to the Bi dopant atoms. However, plotting the Mn $L_{2,3}$ intensity ratio, which correlates with the 3D-band occupation, i.e. the formal oxidation state, reveals *stripes*. Figure 15b compares EELS spectra from the parent compounds $CaMnO_3$ and $LaMnO_3$, with Mn in +4 and +3 oxidation states, respectively, to spectra obtained from selected columns in the BCMO. Figure 15c shows a line scan of the $L_{2,3}$ intensity ratio along the ⟨100⟩ pseudocubic direction where it is very clear that the Mn oxidation state jumps from +4 to +3 along the directions of the arrow. The jumps occur every three or four Mn planes, consistent with the nominal doping level of $x = 0.37$ [65].

In this case, the change in the Mn oxidation state due to occupation of the 3D-band induces a Jahn–Teller distortion in the surrounding O sublattice. Any extra charge density due to the additional electron located in the Mn orbital is compensated by this outward motion of surrounding O atoms, and the total charge surrounding every Mn atom (whether in a +4 or +3 oxidation state) remains essentially the same as in Mn metal [66]. In a sharp contrast to the clear striping seen in Fig. 15, EELS studies of the half-doped manganites $Bi_{0.5}(Sr_{0.4}Ca_{0.1})MnO_3$ [67] and $Pr_{0.5}Ca_{0.5}MnO_3$ [68] show minimal oxidation state striping, behavior which is consistent with a Zener polaron model proposed earlier [69,70] where the additional electron splits almost equally between the two Mn sites.

Long-range charge transfer has been seen in a $YBa_2Cu_3O_{7-x}/La_{0.7}Ca_{0.3}MnO_3$ (YBCO/LCMO) ferromagnetic/superconducting oxide heterostructure, see [71]. At each interface, a hole depletion zone was found to extend ~3 nm into the YBCO, with a corresponding depletion of electrons occurring from the LCMO layer. These charge transfers are fully in accord with the measured properties of these superlattices. The magnitude of the charge transfer has also recently been confirmed by X-ray absorption spectroscopy measurements [72], but only the integrated charge could be extracted and not the details of the spatial distributions that STEM/EELS provides.

Figure 16 shows a high-resolution study of the measurement of oxidation states in manganites, using a large enough number of points per unit cell to quantify variations in the apparent oxidation state with the position of the beam in the unit cell [73]. The spectrum image shows clearly the rippling that demonstrates that atomic resolution was achieved in the EELS line scan. In particular, the O *K* edge shows the double periodicity indicative of the volcano structure, which is also seen to a lesser extent on the Mn $L_{2,3}$ edge. The oxidation states were extracted by three different methods, from the $L_{2,3}$ ratio, the normalized ratio of the O *K* prepeak to the main peak and also from their energy separation, all of which are known to reflect the Mn oxidation state. However, the different methods showed different sensitivities to probe position, which are not presently understood. The most reliable method for extracting oxidation states was found to be the energy separation method, which, furthermore, in conjunction with dynamical image simulations and first-principles calculations are capable of identifying the inequivalent O sites induced by the Jahn–Teller distortions [73].

While many of the variations in experimental oxidation state are close to the error bars of the measurement, with

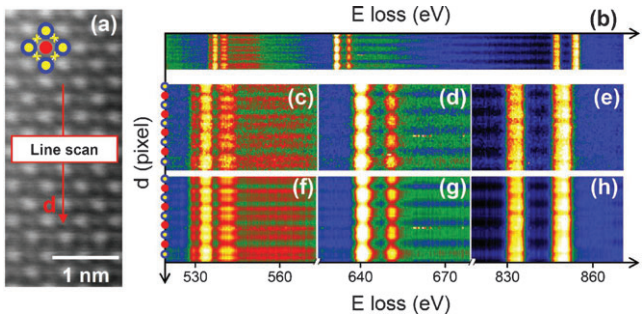

Fig. 16. (a) *Z*-contrast image of a $LaMnO_3$ sample viewed down the pseudocubic ⟨100⟩ zone axis. A pseudocubic unit cell is marked, with a red circle marking the La column position, and blue/yellow circles showing the Mn–O columns. Yellow crosses mark the approximate positions of pure O columns between Mn–O columns. (b) EELS line scan acquired along the direction of the red arrow in (a). (c, d and e) Magnified portions of (b), showing the O *K*, the Mn $L_{2,3}$ and the La $M_{4,5}$ edges, respectively. (f, g and h) O *K*, Mn $L_{2,3}$ and La $M_{4,5}$ edge images in (c, d and e), respectively, after principal component analysis [77] to reduce noise. All of the EELS images show the rippling characteristic of atomic-resolution EELS. The O *K* image shows a double ripple, characteristic of the volcano (as does the La $M_{4,5}$ image, although the contrast is not so strong). For figures (c–h) the approximate position of the La (Mn–O) columns is highlighted on the left with red (blue-yellow) circles. Data recorded with the VG Microscopes HB501UX equipped with Nion aberration corrector and Gatan Enfina PEELS system, reproduced from [73].

the next generation of microscopes the error bars will be reduced, and these experiments highlight the need for a better theoretical understanding of STEM fine structure imaging. Present dynamical image simulations do not include any EELS fine structure in the calculation, treating the atoms as a lattice of non-interacting (unbonded) atoms. First-principles calculations, although capable of including the core hole effect, assume plane wave illumination, which is appropriate for X-ray excitation but not for the highly convergent, coherent probe in the STEM. Recent work [74,75] has shown the importance of coherent interference terms in ionization, and therefore it is apparent that such effects must be investigated in the context of imaging.

Summary

Atomic-resolution spectroscopy has progressed far from the first inception in 1993 to today, when we are looking forward to a full 2D spectroscopic analysis of electronic structure at sub-unit cell resolution, and in principle, with resolution also in the third dimension. Spectroscopic imaging in the STEM seems to be set on a course to complement the scanning tunneling microscope, with the ability to probe subsurface electronic structure inside real materials and at their internal interfaces to provide a new level of insight into the origin of materials properties.

It is interesting to reflect on the impact that instrumental development has had on the practical application of atomic-resolution EELS. The CCD-based parallel detection system was critical to the demonstration of atomic-resolution EELS in 1993. The successful implementation of aberration correction allows EELS data to be obtained with 100% collection efficiency so that the ultimate limits of the analysis are set now only by the beam specimen interaction. Whether a high or low accelerating voltage is optimum probably depends on the nature of the specimen, in particular, its sensitivity to different damage mechanisms. Higher voltages create knock-on damage, while lower voltages enhance ionization damage but also lead to a higher EELS signal.

What is clear is that with modern microscopes, the intrinsic benefits of STEM for simultaneous imaging of atomic and electronic structure have indeed progressed from a dream limited by noise to a practical reality waiting for applications.

Acknowledgements

The authors would like to thank L. J. Allen for helpful discussions, and their collaborators in the work reviewed here, N. D. Browning, M. M. McGibbon, E. C. Dickey, V. P. Dravid, P. D. Nellist, D. J. Wallis, G. Duscher, S. D. Findlay, H. M. Christen, A. Y. Borisevich, N. Dellby, O. L. Krivanek, L. J. Allen, T. J. Pennycook, K. van Benthem, A. J. D'Alfonso, M. F. Murfitt, Z. S. Szilagyi, R. Jin, B. Sales, D. G. Mandrus, W. Luo, M. Watanabe, J. Tao, S. T. Pantelides, W. H. Sides and J. T. Luck, which was supported by the Division of Materials Sciences and Engineering, USDOE and in part by the Laboratory Directed Research and Development Program of ORNL.

References

1 Crewe A V, and Wall J (1970) A scanning microscope with 5 Å resolution. *J. Mol. Biol.* **48**:375–393.

2 Ritchie R H, and Howie A (1988) Inelastic-scattering probabilities in scanning-transmission electron-microscopy. *Philos. Mag. A* **58**:753–767.

3 Rose H (1976) Image formation by inelastically scattered electrons in electron microscopy. *Optik* **45**:139–158, 187–208.

4 Varela M, Findlay S D, Lupini A R, Christen H M, Borisevich A Y, Dellby N, Krivanek O L, Nellist P D, Oxley M P, Allen L J, and Pennycook S J (2004) Spectroscopic imaging of single atoms within a bulk solid. *Phys. Rev. Lett.* **92**:095502.

5 Borisevich A Y, Lupini A R, and Pennycook S J (2006) Depth sectioning with the aberration-corrected scanning transmission electron microscope. *Proc. Nat. Acad. Sci. USA* **103**:3044–3048.

6 Borisevich A Y, Lupini A R, Travaglini S, and Pennycook S J (2006) Depth sectioning of aligned crystals with the aberration-corrected scanning transmission electron microscope. *J. Electron Microsc.* **55**:7–12.

7 van Benthem K, Lupini A R, Kim M, Baik H S, Doh S, Lee J H, Oxley M P, Findlay S D, Allen L J, Luck J T, and Pennycook S J (2005) Three-dimensional imaging of individual hafnium atoms inside a semiconductor device. *Appl. Phys. Lett.* **87**:034104.

8 van Benthem K, Lupini A R, Oxley M P, Findlay S D, Allen L J, and Pennycook S J (2006) Three-dimensional ADF imaging of individual atoms by through-focal series scanning transmission electron microscopy. *Ultramicroscopy* **106**:1062–1068.

9 D'Alfonso A J, Findlay S D, Oxley M P, Pennycook S J, van Benthem K, and Allen L J (2007) Depth sectioning in scanning transmission electron microscopy based on core-loss spectroscopy. *Ultramicroscopy* **108**:17–28.

10 Nellist P D, Behan G, Kirkland A I, and Hetherington C J D (2006) Confocal operation of a transmission electron microscope with two aberration correctors. *Appl. Phys. Lett.* **89**:124105.

11 Cosgriff E C, and Nellist P D (2007) A Bloch wave analysis of optical sectioning in aberration-corrected STEM. *Ultramicroscopy* **107**:626–634.

12 Nellist P D, Cosgriff E C, Behan G, and Kirkland A I (2008) Imaging modes for scanning confocal electron microscopy in a double aberration-corrected transmission electron microscope. *Microsc. Microanal.* **14**:82–88.

13 Reimer L (1985) *Scanning Electron Microscopy* (Springer, Berlin).

14 Cherns D, Hetherington C J D, and Humphreys C J (1984) The atomic structure of the $NiSi_2$-(001)Si interface. *Philos. Mag. A* **49**:165–177.

15 Cherns D, Anstis G R, Hutchison J L, and Spence J C H (1982) Atomic structure of the $NiSi_2$/(111)Si interface. *Philos. Mag. A* **46**:849–862.

16 Tung R T, Gibson J M, and Poate J M (1983) Formation of ultrathin single-crystal silicide films on Si: surface and interfacial stabilization of Si-$NiSi_2$ epitaxial structures. *Phys. Rev. Lett.* **50**:429.

17 Werner P, Jager W, and Schuppen A (1993) Interface structure and Schottky barrier height of buried $CoSi_2$/Si(001) layers. *J. Appl. Phys.* **74**:3846–3854.

18 Bulle-Lieuwma C W T, Jong A F, Ommen A H, Veen J F, and Vrijmoeth J (1989) Determination of the coordination number of Co atoms at the $CoSi_2$(A,B)/Si(111) interface by transmission electron microscopy. *Appl. Phys. Lett.* **55**:648–650.

19 Gibson J M, Bean J C, Poate J M, and Tung R T (1982) Direct determination of atomic structure at the epitaxial cobalt disilicide on (111) Si interface by ultrahigh resolution electron microscopy. *Appl. Phys. Lett.* **41**:818–820.

20 Mantl S (1992) Ion beam synthesis of epitaxial silicides: fabrication, characterization and applications. *Mater. Sci. Rep.* **8**:1–95.

21 Falke M, Falke U, Bleloch A, Teichert S, Beddies G, and Hinneberg H J (2005) Real structure of the CoSi2/Si(001) interface studied by dedicated aberration-corrected scanning transmission electron microscopy. *Appl. Phys. Lett.* **86**:203103.

22 Browning N D, Chisholm M F, and Pennycook S J (1993) Atomic-resolution chemical-analysis using a scanning-transmission electron-microscope. *Nature* **366**:143–146.

23 McMullan D, Rodenburg J M, Murooka Y, and McGibbon A J (1990) Parallel EELS CCD detector for a VG HB501 STEM. *Inst. Phys. Conf. Ser.* 55–58.

24 Browning N D, McGibbon M M, Chisholm M F, and Pennycook S J (1993) Atomic-resolution characterization of interface structures by electron energy loss spectroscopy. In: *51st Annual Proceedings of the Microscopy Society of America*, pp 576–577 (San Francisco Press San Francisco, CA, USA).

25 Berger S D, and Pennycook S J (1982) Detection of nitrogen at (100) platelets in diamond. *Nature* **298**:635–637.

26 Browning N D, Chisholm M F, and Pennycook S J (2006) Atomic-resolution chemical analysis using a scanning transmission electron microscope (vol. 366, p 143, 1993). *Nature* **444**:235.

27 Egerton R F (1996) *Electron Energy-Loss Spectroscopy in the Electron Microscope* (Plenum, New York).

28 Allen L J, Findlay S D, Oxley M P, and Rossouw C J (2003) Lattice-resolution contrast from a focused coherent electron probe. Part I. *Ultramicroscopy* **96**:47–63.

29 Browning N D, Chisholm M F, and Pennycook S J (1993) Atomic-resolution electron energy loss spectroscopy in the scanning transmission electron microscope. In: *27th Annual Proceedings of the Microbeam Analysis Society*, pp S270–S271 (VCH, Los Angeles, CA, USA).

30 Dickey E C, Dravid V P, Nellist P D, Wallis D J, and Pennycook S J (1998) Three-dimensional atomic structure of NiO-ZrO_2(cubic) interfaces. *Acta Mater.* **46**:1801–1816.

31 Mkhoyan K A, Kirkland E J, Silcox J, and Alldredge E S (2004) Atomic level scanning transmission electron microscopy characterization of GaN/AlN quantum wells. *J. Appl. Phys.* **96**:738–746.

32 Batson P E (1993) Simultaneous STEM imaging and electron energy-loss spectroscopy with atomic-column sensitivity. *Nature* **366**:727–728.

33 Kohl H, and Rose H (1985) Theory of image-formation by inelastically scattered electrons in the electron-microscope. *Adv. Imaging Electron Phys.* **65**:173–227.

34 Muller D A, Tzou Y, Raj R, and Silcox J (1993) Mapping Sp(2) and Sp(3) states of carbon at subnanometer spatial-resolution. *Nature* **366**:725–727.

35 McGibbon A J, Pennycook S J, and Angelo J E (1995) Direct observation of dislocation core structures in CdTe/GaAs(001). *Science* **269**:519–521.

36 Pennycook S J, Chisholm M F, Yan Y, Duscher G, and Pantelides S T (1999) A combined experimental and theoretical approach to grain boundary structure and segregation. *Physica B* **274**:453–457.

37 Wallis D J, Browning N D, Nellist P D, Pennycook S J, Majid I, Liu Y, and VanderSande J B (1997) Atomic structure of a 36.8 (210) tilt grain boundary in TiO_2. *J. Am. Ceram. Soc.* **80**:499–502.

38 Duscher G, Browning N D, and Pennycook S J (1998) Atomic column resolved electron energy-loss spectroscopy. *Phys. Status Solidi A* **166**:327–342.

39 Kurata H, and Colliex C (1993) Electron-energy-loss core-edge structures in manganese oxides. *Phys. Rev. B* **48**:2102–2108.

40 Leapman R D, and Grunes L A (1980) Anomalous L_3-L_2 white-line ratios in the 3d transition-metals. *Phys. Rev. Lett.* **45**:397–401.

41 Leapman R D, Grunes L A, and Fejes P L (1982) Study of the L_{23} edges in the 3d transition-metals and their oxides by electron-energy-loss spectroscopy with comparisons to theory. *Phys. Rev. B* **26**:614–635.

42 Paterson J H, and Krivanek O L (1990) ELNES of 3d transition-metal oxides: 2. Variations with oxidation-state and crystal-structure. *Ultramicroscopy* **32**:319–325.

43 Pearson D H, Ahn C C, and Fultz B (1993) White lines and d-electron occupancies for the 3d and 4d transition-metals. *Phys. Rev. B* **47**:8471–8478.

44 Kim M, Duscher G, Browning N D, Sohlberg K, Pantelides S T, and Pennycook S J (2001) Nonstoichiometry and the electrical activity of grain boundaries in $SrTiO_3$. *Phys. Rev. Lett.* **86**:4056–4059.

45 Batson P E, Dellby N, and Krivanek O L (2002) Sub-angstrom resolution using aberration corrected electron optics. *Nature* **418**:617–620.

46 Klie R F, Buban J P, Varela M, Franceschetti A, Jooss C, Zhu Y, Browning N D, Pantelides S T, and Pennycook S J (2005) Enhanced current transport at grain boundaries in high-Tc superconductors. *Nature* **435**:475–478.

47 Chaudhari P, Mannhart J, Dimos D, Tsuei C C, Chi J, Oprysko M M, and Scheuermann M (1988) Direct measurement of the superconducting properties of single grain-boundaries in $YBa_2Cu_3O_{7-\delta}$. *Phys. Rev. Lett.* **60**:1653–1656.

48 Dimos D, Chaudhari P, and Mannhart J (1990) Superconducting transport-properties of grain-boundaries in $YBa_2Cu_3O_{7-\delta}$ bicrystals. *Phys. Rev. B* **41**:4038–4049.

49 Dimos D, Chaudhari P, Mannhart J, and Legoues F K (1988) Orientation dependence of grain-boundary critical currents in $YBa_2Cu_3O_{7-\delta}$ bicrystals. *Phys. Rev. Lett.* **61**:219–222.

50 McGibbon M M, Browning N D, McGibbon A J, and Pennycook S J (1996) The atomic structure of asymmetric [001] tilt boundaries in $SrTiO_3$. *Philos. Mag. A* **73**:625–641.

51 Browning N D, Buban J P, Nellist P D, Norton D P, Chisholm M F, and Pennycook S J (1998) The atomic origins of reduced critical currents at [001] tilt grain boundaries in $YBa_2Cu_3O_{7-\delta}$ thin films. *Physica C* **294**:183–193.

52 Browning N D, Buban J P, Prouteau C, Duscher G, and Pennycook S J (1999) Investigating the atomic scale structure and chemistry of grain boundaries in high-Tc superconductors. *Micron* **30**:425–436.

53 Song X, Daniels G D, Feldmann M, Gurevich A, and Larbalestier D (2005) Electromagnetic, atomic structure and chemistry changes induced by Ca-doping of low-angle $YBa_2Cu_3O_{7-\delta}$ grain boundaries. *Nat. Mat* **4**:470–475.

54 Browning N D, Yuan J, and Brown L M (1992) Determination of the local oxygen stoichiometry in $YBa_2Cu_3O_{7-\delta}$ by electron-energy loss spectroscopy in the scanning- transmission electron-microscope. *Physica C* **202**:12–18.

55 Krivanek O L, Dellby N, Keyse R J, Murfitt M F, Own C S, and Szilagyi Z S (2008) In: Hawkes P W (ed.), *Aberration-Corrected Electron Microscopy* pp 121–160 (Academic Press, New York).

56 Suenaga K, Tence T, Mory C, Colliex C, Kato H, Okazaki T, Shinohara H, Hirahara K, Bandow S, and Iijima S (2000) Element-selective single atom imaging. *Science* **290**:2280–2282.

57 Lupini A R and Pennycook S J (2003) Localization in elastic and inelastic scattering. *Ultramicroscopy* **96**:313–322.

58 Oxley M P, Varela M, Pennycook T J, van Benthem K, Findlay S D, D'Alfonso A J, Allen L J, and Pennycook S J (2007) Interpreting atomic-resolution spectroscopic images. *Phys. Rev. B* **76**:064303.

59 Hytch M J, and Stobbs W M (1994) Quantitative comparison of high-resolution TEM images with image simulations. *Ultramicroscopy* **53**:191–203.

60 Egerton R F (2007) Limits to the spatial, energy and momentum resolution of electron energy-loss spectroscopy. *Ultramicroscopy* **107**:575–586.

61 D'Alfonso A J, Findlay S D, Oxley M P, and Allen L J (2008) Volcano structure in atomic resolution core-loss images. *Ultramicroscopy* **108**:677–687.

62 Bosman M, Keast, V J, Garcia-Munoz, J L, D'Alfonso A J, Findlay S D, and Allen L J (2007) Two-dimensional mapping of chemical information at atomic resolution. *Phys. Rev. Lett.* **99**:086102.

63 Kimoto K, Asaka T, Nagai T, Saito M, Matsui Y, and Ishizuka K (2007) Element-selective imaging of atomic columns in a crystal using STEM and EELS. *Nature* **450**:702–704.

64 Muller D A, Kourkoutis L F, Murfitt M, Song J H, Hwang H Y, Silcox J, Dellby N, and Krivanek O L (2008) Atomic-scale chemical imaging of composition and bonding by aberration-corrected microscopy. *Science* **319**:1073–1076.

65 Varela M, Lupini A R, van Benthem K, Borisevich A, Chisholm M F, Shibata N, Abe E, and Pennycook S J (2005) Materials Characterization in the aberration-corrected scanning transmission electron microscope. *Annu. Rev. Mater. Res.* **35**: 539–569.

66 Luo W, Franceschetti A, Varela M, Tao J, Pennycook S J, and Pantelides S T (2007) Orbital-occupancy versus charge ordering and the strength of electron correlations in electron-doped $CaMnO_3$. *Phys. Rev. Lett.* **99**:036402.

67 Loudon J C, Kourkoutis L F, Ahn J S, Zhang C L, Cheong S W, and Muller D A (2007) Valence changes and structural distortions in "charge ordered" manganites quantified by atomic-scale scanning transmission electron microscopy. *Phys. Rev. Lett.* **99**:237205.

68 Wu L, Klie, R F, Zhu Y, and Jooss C (2007) Experimental confirmation of Zener-polaron-type charge and orbital ordering in $Pr_{1-x}Ca_xMnO_3$. *Phys. Rev. B* **76**.

69 Daoud-Aladine A, Rodriguez-Carvajal J, Pinsard-Gaudart L, Fernandez-Diaz M T, and Revcolevschi A (2002) Zener polaron ordering in half-doped manganites. *Phys. Rev. Lett.* **89**:097205.

70 Hejtmanek J, Knizek K, Jirak Z, Hervieu M, Martin C, Nevriva M, and Beran P (2003) Ordering phenomena and transport properties of $Bi_{1/2}Sr_{1/2}$ MnO_3single crystals. *J. Appl. Phys.* **93**:7370–7372.

71 Varela M, Lupini A R, Peña V, Sefrioui Z, Arslan I, Browning N D, Santamaria J, and Pennycook S J (2005) Direct measurement of charge transfer phenomena at ferromagnetic/superconducting oxide interfaces. http://arxiv.org/pdf/cond-mat/0508564v2.

72 Chakhalian J, Freeland J W, Habermeier H U, Cristiani G, Khaliullin G, van Veenendaal M, and Keimer B (2007) Orbital reconstruction and covalent bonding at an oxide interface. *Science* **318**:1114–1117.

73 Varela M, Luo W, Tao J, Oxley M P, Watanabe M, Lupini A R, Pantelides S T, and Pennycook S J (2008) Atomic resolution imaging of oxidation states in manganites. Unpublished paper.

74 Allen L J, Findlay S D, Oxley M P, Witte C, and Zaluzec N J (2006) Channeling effects in high-angular-resolution electron spectroscopy. *Phys. Rev. B* **73**:094104.

75 Schattschneider P, Hebert C, and Jouffrey B (2001) Orientation dependence of ionization edges in EELS. *Ultramicroscopy* **86**:343–353.

76 Varela M, Gazquez J, Lupini A R, Luck J T, Torija M A, Sharma M, Leighton C, Biegalski M D, Christen H M, Murfitt M F, Dellby N, Krivanek O L, and Pennycook S J (2008) Applications of aberration corrected scanning transmission electron microscopy and electron energy loss spectroscopy to thin oxide films and interfaces. *Zeitschrift fur Metallkunde*, in press.

77 Bosman M, Watanabe M, Alexander D T L, and Keast V J (2006) Mapping chemical and bonding information using multivariate analysis of electron energy-loss spectrum images. *Ultramicroscopy* **106**:1024–1032.